This is the accepted manuscript made available via CHORUS. The article has been published as:

Complementary Vanadium Dioxide Metamaterial with Enhanced Modulation Amplitude at Terahertz Frequencies

Yuwei Huang, Xuefei Wu, Jacob Schalch, Guangwu Duan, Chunxu Chen, Xiaoguang Zhao, Kelson Kaj, Hai-Tian Zhang, Roman Engel-Herbert, Richard D. Averitt, and Xin Zhang

Phys. Rev. Applied **18**, 054086 — Published 29 November 2022

DOI: 10.1103/PhysRevApplied.18.054086

Complementary Vanadium Dioxide Metamaterial with Enhanced Modulation Amplitude at Terahertz Frequencies

Yuwei Huang,[1,*] Xuefei Wu,[1,*] Jacob Schalch,[2] Guangwu Duan,[1] Chunxu Chen,[1] Xiaoguang Zhao,[1] Kelson Kaj,[2] Hai-Tian Zhang,[3] Roman Engel-Herbert,[3,4] Richard D. Averitt,[2,†] and Xin Zhang[1,‡]

[1]*Department of Mechanical Engineering and Division of Materials Science and Engineering, Boston University, Boston, Massachusetts 02215, USA*

[2]*Department of Physics, University of California, San Diego, La Jolla, California 92903, USA*

[3]*Department of Materials Science and Engineering, the Pennsylvania State University, University Park, Pennsylvania 16802, USA*

[4]*Paul-Drude-Institut fr Festkrperelektronik, Leibniz-Institut im Forschungsverbund Berlin e.V., Hausvogteiplatz 5-7, 10117 Berlin, Germany*

(Dated: November 1, 2022)

One route to create tunable metamaterials is through integration with on-demand dynamic quantum materials, such as vanadium dioxide (VO_2). This enables modalities to create high performance devices for historically challenging applications. Indeed, dynamic materials have often been integrated with metamaterials to imbue artificial structures with some degree of tunability. Conversely, metamaterials can be used to enhance and extend the natural tuning range of dynamic materials. Utilizing a complementary split ring resonator array deposited on a VO_2 film, we demonstrate enhanced terahertz transmission modulation upon traversing the insulator-to-metal transition (IMT) at ∼340 K. Our complementary metamaterial increases the modulation amplitude of the original VO_2 film from 0.42 to 0.68 at 0.47 THz upon crossing the IMT, corresponding to an enhancement of 62%. Moreover, temperature dependent transmission measurements reveal a significant redshift of the resonant frequency in a narrow temperature range where phase coexistence is known to occur. Neither Maxwell-Garnett nor Bruggeman effective medium theory adequately describes the observed frequency shift and amplitude decrease. However, a Drude model incorporating a significant increase of the effective permittivity does describe the experimentally observed redshift. Our results highlight that symbiotic integration of metamaterial arrays with quantum materials provides a powerful approach to engineer emergent functionality.

I. INTRODUCTION

Metamaterials, and their single layer analogs (metasurfaces), have enabled a plethora of applications and devices by overcoming the limitations of natural materials. This includes subwavelength imaging [1], the realization of a negative refractive index [2], near zero epsilon devices [3], and the demonstration of cloaks and metalenses [4, 5]. Building on these capabilities, active control and tunability in metamaterials could lead to modulators, switches, and sensors over a vast span of the electromagnetic spectrum [6–10].

Vanadium dioxide (VO_2) is a tunable quantum material that has been extensively investigated (in large part) because the insulator-to-metal transition (IMT) occurs above room temperature at ∼340 K [11]. Light, current, and mechanical strain can also drive the IMT, making VO_2 useful for a broad range of applications [8, 12–16]. Upon undergoing the IMT, the optical conductivity changes by four-orders of magnitude over a broad spectral range, making VO_2 a versatile material to integrate with metamaterials to realize nonlinear responses, state switches, and modulators [17, 18]. Recent efforts have focused on combining VO_2 with metamaterials in the terahertz (THz) frequency range to realize switchable broadband absorbers, tunable coding and multi-functional devices based on the IMT [19–22].

In order to enhance the THz response and explore the phase transition behavior of VO_2, we deposited a metamaterial array of complementary split ring resonators (SRRs) on a thin film using direct laser writing and photolithography. As described below, the resultant structure exhibits a significantly enhanced THz transmission modulation across the IMT in excess of a pristine VO_2 film. Moreover, these results highlight that, in some cases, complementary SRRs enable operational modalities not possible with standard SRRs (e.g., see Fig. 9 for a comparison). Previous studies have demonstrated transmission modulation, but suffer from a high insertion loss (> 40%)[23] or a relatively small amplitude modulation enhancement in comparison to a pristine film [16].

In addition to the functional increase of the THz transmission modulation upon traversing the IMT, the sensitivity of the metamaterial resonators to the surrounding dielectric environment reveals an abnormally large increase of the permittivity of VO_2 during the IMT. This phenomenon can be attributed to insulating and metallic phase coexistence at the onset of the IMT, which has previously been studied by scanning near-field infrared microscopy [24–26]. With increasing temperature, the formation of rutile metallic puddles surrounded by an in-

* These two authors contributed equally
† raveritt@ucsd.edu
‡ xinz@bu.edu

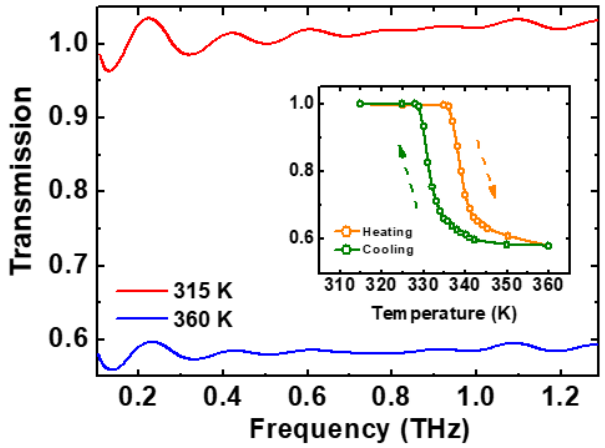


FIG. 1. (a) Terahertz transmission amplitude versus frequency of the pristine VO_2 film in the monoclinic insulating state (red line, 315 K) and rutile metallic phase (blue line, 360 K). Inset is the THz transmission (at 0.47 THz) of the VO_2 film as a function of temperature across the IMT transition. The expected hysteresis is observed upon heating (orange dots) and cooling (green dots) with lines to guide the eye.

sulating VO_2 matrix results in an increase in the effective permittivity, as typically described by Maxwell-Garnett effective medium theory (MG-EMT) [27] and Bruggeman effective medium theory (BG-EMT)[28]. Our results indicate that neither MG-EMT nor BG-EMT accurately describe the experimentally observed resonance redshift. Instead, we employed the Drude model with a significant increase of the effective permittivity to describe the redshift of the resonance upon traversing the IMT [29]. In the following, we describe the transmission enhancement properties of integrated metamaterial VO_2 films. Our results highlight the functionality of metamaterial–quantum material hybrid structures and demonstrate that complementary SRRs can be used to interrogate mesoscopic phase transitions.

II. COMPLEMENTARY VANADIUM DIOXIDE METAMATERIAL

A. Terahertz transmission of pristine vanadium dioxide film

The VO_2 film was deposited on a sapphire substrate by hybrid molecular beam epitaxy using combinatorial growth [30, 31]. Details of the film growth process can be found in Appendix A. The frequency dependent transmission was measured using THz time domain spectroscopy (THz-TDS) [32]. THz pulses were generated using near infrared (800 nm) pulses generated by a Ti:sapphire laser with a pulse duration of 25 fs. The pulses illuminate a biased photoconductive antenna, and are detected using a similar photoconductive antenna gated by the 800 nm pulses.

THz-TDS transmission measurements of the pristine VO_2 film were performed prior to metamaterial integration. Fig. 1(a) shows the transmission of the VO_2 film at 315 K in the insulating monoclinic phase and at 360 K in the rutile metallic phase (T_c ∼340 K). Near unity transparency is observed close to room temperature for a 65 nm thick VO_2 film in the insulating state (we note that the transmission is referenced to a bare sapphire substrate). Referencing errors caused by birefringent mismatch between the sample and substrate reference along with artifacts arising from an etalon in the sapphire substrates results in small oscillations in the transmission above unity at some frequencies. In the metallic state, the transmission decreases to 0.58. This corresponds to a 0.42 transmission amplitude modulation between the insulating and metallic state. We note that the flat spectral response in the metallic state arises from the short quasiparticles scattering time. The temperature dependent transmission amplitude at 0.47 THz is shown in the inset of Fig. 1. Hysteresis upon heating and cooling is observed as expected for a first order phase transition. Fitting the first derivative of the hysteresis loop to a Gaussian yields a transition temperature with heating of 339 K, and with cooling of ∼330 K, corresponding to a hysteresis width of 9 K. This dynamic change of transmission under different temperatures makes VO_2 a potential material for tunable THz bandpass filters [33, 34].

B. Design, simulations, and experimental results

Metallic SRR metamaterials exhibit a LC dipole resonance that can modify the transmission modulation of the VO_2 film. For a conventional (i.e., not complementary) SRR array on top of a VO_2 film, there is a dip in transmission in the insulating state at the SRR resonance frequency (see Appendix B, Fig. 9(a)). Upon traversing the IMT, the transmission will increase since the capacitive gaps of the SRRs are shorted by the metallic VO_2. In this case, the modulation depth is considerably smaller as compared to the pristine VO_2 film. However, based on Babinets principle [35, 36], a complementary SRR structure exhibits a peak in transmission due to the resonance in the insulating state of VO_2 which can be expected to decrease in the metallic state. Therefore, we investigate the transmission modulation of complementary SRRs integrated with a VO_2 film for enhanced transmission modulation. An array of complementary split ring resonators (CSRRs) was deposited on a VO_2 film using direct laser writing and photolithography to construct a CSRR-VO_2 metamaterial (CSRR-VO_2 MM). Fig. 2(a) shows an optical image of the array. A 150 nm thick gold film (with a 10 nm Ti adhesion layer) was deposited on the VO_2 film. The lateral dimension of the CSRR is 45 μm with a periodicity of 50 μm, a linewidth of 5 μm, and slit widths of 3 μm on both branches. The frequency dependent transmission amplitude of the CSRR-VO_2 MM measured

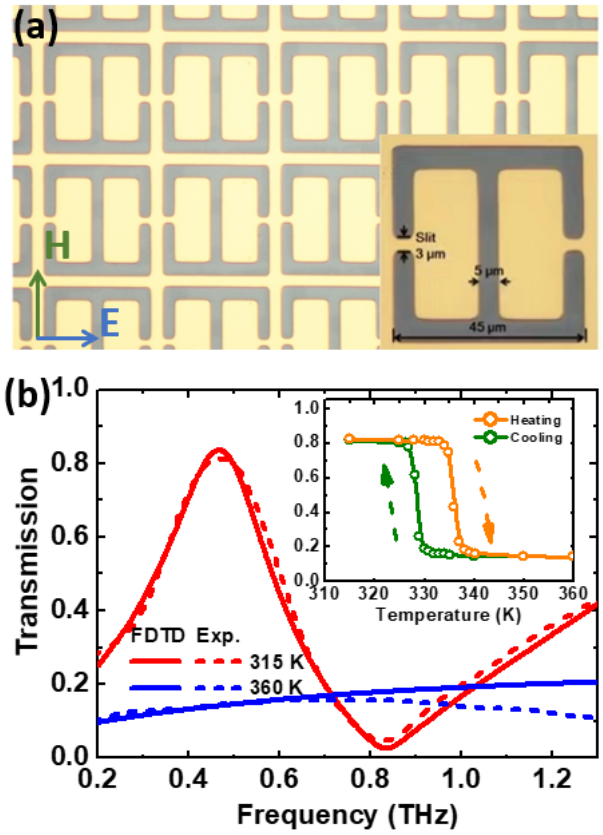


FIG. 2. (a) Microscope image of the CSRR-VO_2 MM on VO_2 film where the inset shows the dimensions of the unit cell. (b) Experimental data (dashed lines) and simulations (solid lines) of the THz transmission of CSRR-VO_2 MM at 315 K (red) and 360 K (blue). Inset is the measurement of temperature-dependent transmission of CSRR-VO_2 MM at 0.47 THz. The solid lines in the inset are a guide to the eye.

using THz-TDS is plotted as dashed lines in Fig. 2(b). The resonance peak occurs at 0.47 THz when the incident light is polarized parallel to the middle gap at 315 K, shown as the blue arrow in Fig. 2(a). The transmission amplitude is 0.83 (compared to the pristine VO_2 films, corresponding to an insertion loss of 17% – nonetheless the transmission is reasonably high). Conversely, upon fully traversing to the metallic state to 360 K, no resonant transmission response is evident (blue line, Fig. 2(b)), and the transmission is 0.15 at 0.47 THz. Thus, the modulation amplitude of the THz transmission at 0.47 THz upon crossing the IMT is 0.68, an increase of 62% relative to the bare VO_2 (Fig. 1). Numerical simulations of the electromagnetic response of the CSRR-VO_2 MM were performed using CST Microwave Studio. The conductivity of gold was taken as 4.510^7 S/m. In the insulating state, the VO_2 was modeled using a Drude response with the complex permittivity given by [37, 38]:

$$\varepsilon(\omega) = \varepsilon_\infty - \frac{\omega_p^2}{\omega(\omega + i\gamma)} \qquad (1)$$

where the unscreened plasma frequency ω_p is given by $\sqrt{n_d e^2/(\varepsilon_0 m*)}$, n_d is the carrier density, e is electron charge, ε_0 is the free space permittivity, m^* is the carrier effective mass, γ is the scattering frequency ($\gamma = e/\mu m^*$, where μ is the mobility), and ε_∞=10 is the high frequency permittivity. The parameters used in the simulations are shown in Table 1 and the corresponding simulation results are shown as red solid lines in Fig. 2(b). For the metallic state of VO_2, an equivalent carrier density of 1.510^{21} cm^{-3} at 360 K was used as determined from the THz-TDS measurements of the VO_2 film shown in Fig. 1. The parameters for both the insulating and metallic states in Table 1 are consistent with those in published work [8]. Good agreement with experiment is obtained (Fig. 2(b)) in the metallic state, with a simulated transmission amplitude of 0.15 at 0.47 THz. In addition, the inset in Fig. 2(b) shows the temperature dependence of transmission amplitude at 0.47 THz for the CSRR-VO_2 MM during both heating and cooling. A significant change in the transmission upon heating did not occur until 335 K. Indeed, a dramatic reduction of the transmission occurs within a 2 K span from 335 K to 337 K. Similarly, upon cooling, the transmission recovery occurs at a temperature 5 K lower than the turning point of heating.

The mechanism for the increase in transmission modulation going through the IMT can be partially understood by examining the electric fields and current distributions at the resonant frequencies using full-wave electromagnetic simulations. Fig. 3 shows both the electric field and surface current at the resonant frequency (0.47 THz) when VO_2 is in the insulating state (315 K) and metallic state (360 K). As shown in Fig. 3(a), the electric field in the insulating state is concentrated in the central vertical gap while in the metallic state, this region is electrically shorted, reducing the resonant enhancement of the transmission. The surface currents on the CSRR-VO_2 MM for both states are shown with colored arrows in Fig. 3(c) and (d). The circulating current in Fig. 3(c) is indicative of the lowest energy LC mode of the structure. This is the current path that leads to the enhanced transmission on resonance. However, in the metallic state, the VO_2 film allows current to flow across the central gap, effectively shorting the capacitive region and diminishing the LC mode, as shown in Fig. 3(d), resulting in a low transmission amplitude.

C. Temperature dependence of transmission

Having presented the functional response of the CSRR-VO_2 MM, we now consider the temperature dependence of the transmission upon crossing the IMT in greater detail. Fig. 4(a) and (b) show the experimental transmission spectra at different temperatures during heating and cooling, respectively. Notably, with increased temperature, the resonant frequency dramatically redshifts over a narrow temperature interval, decreasing from 0.47

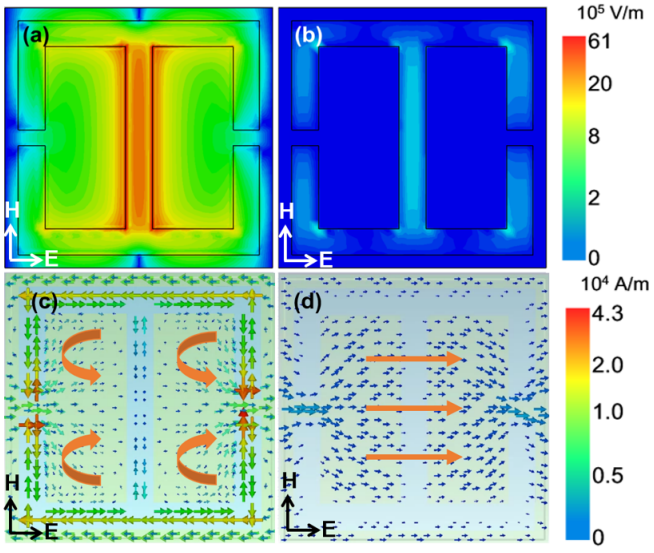


FIG. 3. Simulated electric field of the CSRR-VO_2 MM in the (a) insulating state and (b) metallic state, and the corresponding simulated surface current distributions in the (c) insulating and (d) metallic state at 0.47 THz.

THz at 334 K to 0.38 THz at 336 K, as shown in Fig. 4(a). A further increase of temperature results in a fully screened resonance, leading to a flat transmission spectrum at 338 K and 360 K. Similar blueshifts can also be observed in Fig. 4(b) during cooling after the resonance peak reappears from 328 K to 315 K. To clarify the origin of the resonant frequency shifts, we need to consider the frequency dependent dielectric response of the VO_2 film over the temperature range of the IMT. We first consider two prevalent effective medium theories (EMT). Specifically, Maxwell-Garnett EMT (MG-EMT) and Bruggeman EMT (BG-EMT) [39]:

$$\varepsilon_{eff}^{MG} = \varepsilon_i \frac{\varepsilon_m(1+2f) - \varepsilon_i(2f-2)}{\varepsilon_i(2+f) + \varepsilon_m(1-f)} \tag{2}$$

$$f\frac{\varepsilon_m - \varepsilon_{eff}^{BG}}{\varepsilon_m + 2\varepsilon_{eff}^{BG}} + (1-f)\frac{\varepsilon_i - \varepsilon_{eff}^{BG}}{\varepsilon_i + 2\varepsilon_{eff}^{BG}} = 0 \tag{3}$$

where ε_m and ε_i are the dielectric functions of the metallic and insulating states, respectively, f is the metallic filling factor, and ε_{eff}^{MG} and ε_{eff}^{BG} are the effective dielectric functions based on Maxwell-Garnett and Bruggeman EMT, respectively. We used the ε_m and ε_i at 0.5 THz based on the Drude model with the parameters discussed in Section B (and also in Table 1) and plotted the dielectric function dependence on the metallic filling factors based on the two EMT models, as shown in Fig. 5. The primary difference between the two models is that ε' continuously increases with f and suddenly drops to negative when f >0.95 in MG-EMT while BG-EMT shows the maximum ε' when f is around 0.3.

We used MG-EMT and BG-EMT to obtain dielectric functions under specific filling factors yield the best

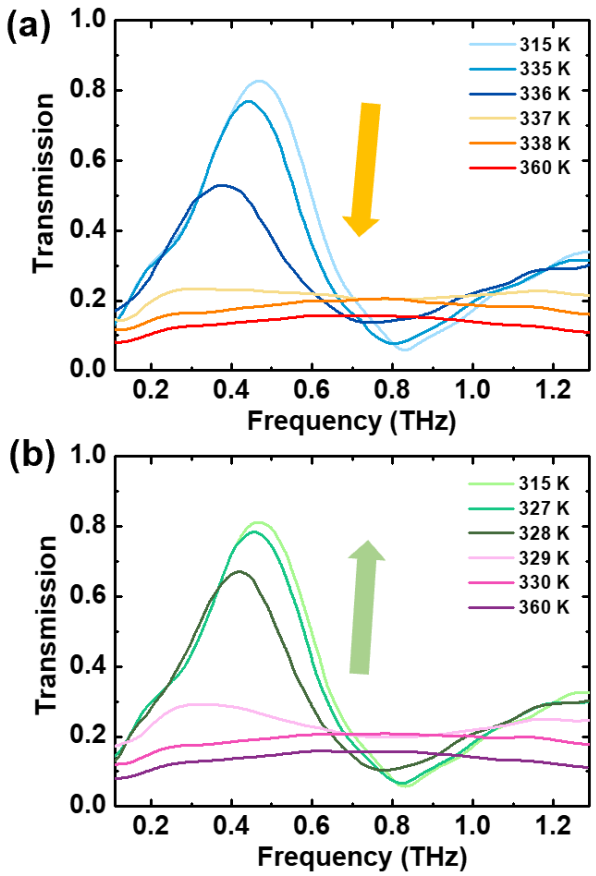


FIG. 4. Experimental transmission spectra of the VO_2 complementary metamaterial upon crossing the IMT during (a) heating and (b) cooling.

match to the experimental terahertz transmission spectra between 335 K and 338 K. Good agreement is obtained for 335 K, 337 K and 338 K for both EMT models, as shown in Appendix C (Fig. 10), but neither model yields a good match at 336 K, as shown in Fig. 6. Specifically, the redshift is greater in experiment than what is obtained from the simulations (the deviation between the experimental and simulation peak frequency, $\Delta F/F_0$, is ∼12% to 17%, as indicated in the insets of Fig. 6). In addition, MG-EMT gives a much higher filling factor (f >0.9) than BG-EMT (f <0.5) between 335 K to 338 K, as shown in insets of Fig. 6 and Fig. 10.

Fig. 7 is a plot of the filling factors (f) and corresponding ε' dependence on temperature for both models. Further fitting of f based on both models based on Boltzmann relationship [28] are shown in Appendix C. As Fig. 7(a) shows, when f is 0.96 in MG-EMT, the permittivity reaches its maximum value, which is almost 30 times of the ε' in the insulating state. Since the Maxwell-Garnett model assumes that the conductive domains are spatially separated, it is not expected to be valid when f is large [29]. Although BG-EMT yields a lower ε' for the corresponding f, the maximum ε' is much lower than the

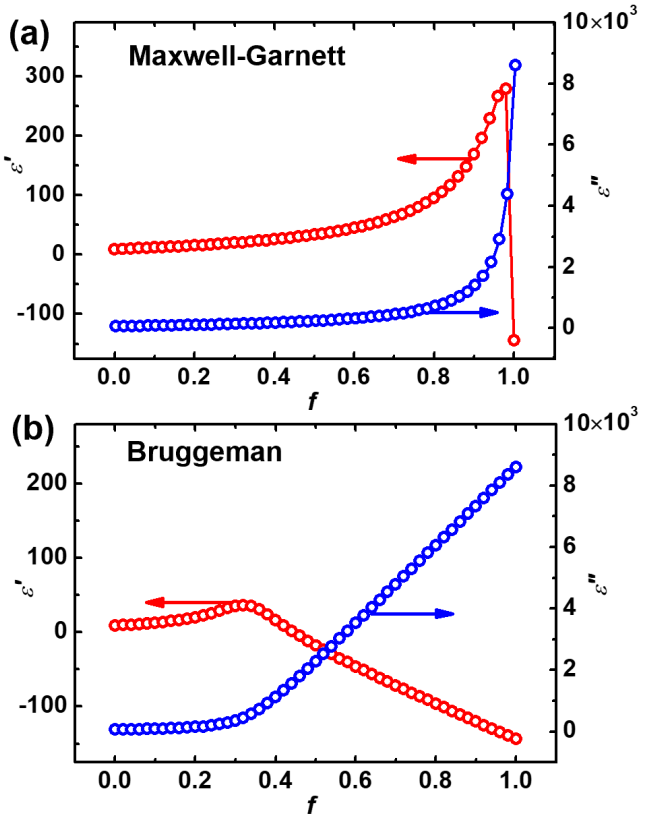


FIG. 5. The real part (ε', red dots) and imaginary part (ε'', blue dots) of the permittivity dependence on the filling factor (f) for (a) Maxwell-Garnett and (b) Bruggeman EMT models.

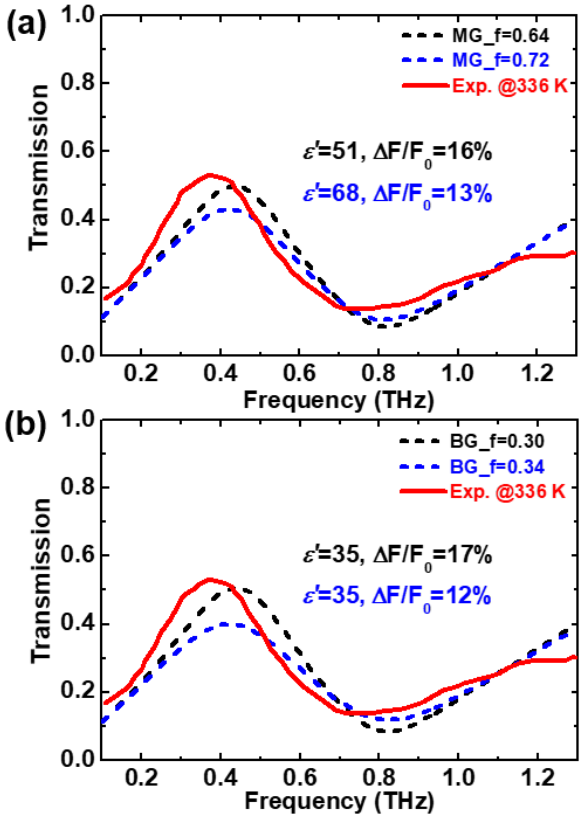


FIG. 6. Comparison between experimental results (red lines) and simulations (dashed lines) for 336K data based on (a) Maxwell-Garnett EMT and (b) Bruggeman EMT. The corresponding filling factors for simulations are also included in the insets.

published experimental work [16, 24, 40]. Moreover, it does not provide a good match of the amplitude decrease and the frequency shift that is experimentally observed at 336 K (Fig. 6(b)).

Since the two EMT models do not adequately fit the experimental amplitude decrease and frequency shift of the resonance mode during IMT, we consider using the Drude model (Eq. (1)) to describe the dielectric properties of VO_2 across the IMT. Based on published work, there is a large change of carrier concentration n_d from $\sim 10^{20}$ cm^{-3} in the insulating state to $\sim 10^{21}$ cm^{-3} in the metallic state, while the mobility μ increases from 1 to 10 cm^2/(V·s), and the effective mass m^* decreases from 7 m_0 to m_0 [41].

We simulated the response with ε_∞ =10 while n, m^* and μ are individually changed, as shown in Fig. 12 (Appendix D). The simulation results reveal that the resonant frequency cannot be tuned over 0.1 THz range observed in experiment while maintaining ε_∞ =10. The deviation of the frequency from the experimental results are between ~9% to 24%. Therefore, we must consider additional effects in the VO_2 film during the IMT. A simple approach is to consider a temperature dependent increase of the CSRR capacitance (that is frequncy independent). This would yield a temperature dependent redshift. Moreover, this is consistent with the notion of enhanced polarizability arising from the metallic domains that arise in the coexistence region of VO_2 [24–26]. This can be accomplished by adding a temperature dependent contribution to ε_∞ to yield an effective static contribution ε_∞^{eff}. Specifically, $\varepsilon_\infty^{eff} = \varepsilon_\infty + \varepsilon^{eff}(T)$.

Fig. 8(a) shows the simulations results using ε_∞^{eff}, using the parameters in Table 1. Simulations using these values capture the redshift of the resonance observed in experiment in Fig. 4(a) (the deviations of peak frequencies between simulations and experimental results are smaller than 1%, as shown in the insets of Fig. 8(a)). We also plotted the corresponding ε' at 0.5 THz based on the Drude parameters in Table 1 at different temperatures in the last column in Table 1. The trend is similar to published work [16, 24, 40] and the two EMT models shown in Fig. 7 although the ε' peak value is much higher. Similar significant permittivity enhancement can also be observed in ferroelectric materials, e.g. $BaTiO_3$ and $CaCu_3Ti_4O_{12}$ due to Maxwell-Wagner relaxation [2, 42–45]. The similar blueshift observed during the cooling process can also be explained by gradually decreasing ε_∞^{eff}, as shown in Fig. 8(b) and Table 1. We also calculated the optical conductivities at ~0.5 THz

TABLE I. Permittivity parameters used for the VO_2 simulations.

Process	Temperature (K)	Electron density (cm^{-3})	Mobility ($cm^2/V{\cdot}s$)	Effective mass (m_0)	ε_∞	$\varepsilon_{0.5THz}$
	315	1.5×10^{20}	1.0	7	10	9
	335	1.9×10^{20}	1.2	6	120	118
Heating	336	3.5×10^{20}	2.0	5	700	692
	337	7.0×10^{20}	6.0	3	10	-67
	338	1.0×10^{21}	7.0	2	10	-90
	360	1.5×10^{21}	10.0	1	10	-144
	330	1.0×10^{21}	7.0	2	10	-90
Cooling	329	5×10^{20}	5.0	3	10	-45
	328	2×10^{20}	1.5	5	350	313
	327	1.7×10^{20}	1.1	6	40	38
	315	1.5×10^{20}	1.0	7	10	9

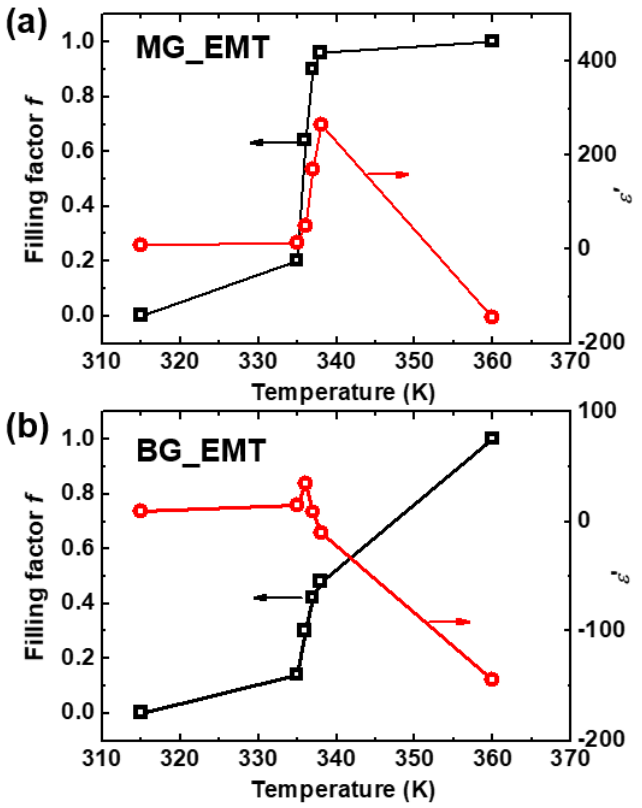


FIG. 7. The temperature dependence of the filling factor f and real part of permittivity (ε') at 0.5 THz based on (a) Maxwell-Garnett EMT and (b) Bruggeman EMT model.

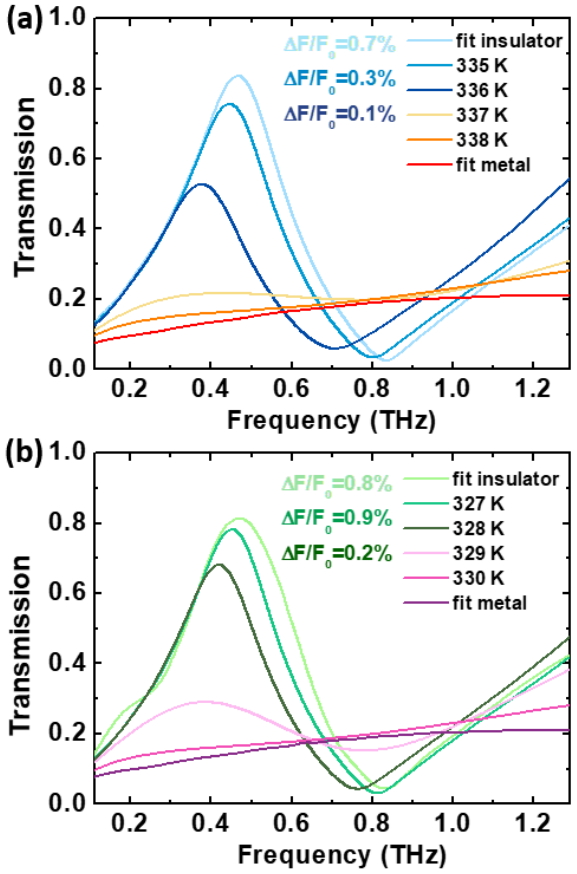


FIG. 8. Numerical simulation spectra of the VO_2 complementary metamaterial upon crossing the IMT during (a) heating and (b) cooling using the values from Table 1. Deviation of the peak frequencies between the simulation and experimental results are also included in the insets (i.e. $\Delta F/F_0$).

(see Appendix E and Fig. 13) and the values are also consistent with published work [24].

Our results indicate that, in addition to the enhancement of the transmission modulation across the IMT, the CSRR MM is highly sensitive to the local permittivity. Unlike the very small capacitive gap in a typical SRR, the central "wire" in the complementary structure acts as the capacitive gap, markedly increasing the area of the resonator which probes the local dielectric environment, thereby increasing the overall sensitivity.

III. CONCLUSION

We demonstrated metamaterial-enhanced dynamic material properties by integrating a complementary split ring resonator metamaterial directly on a VO_2 film. Relative to the IMT in a pristine VO_2 film, the modula-

tion of the THz transmission (peaked at 0.47 THz) of our hybrid device is enhanced by 62%. Moreover, the complementary SRR structure has a larger effective gap area than typical SRR geometries, providing a sensitive probe of the local electrodynamics of the VO_2. With increasing (decreasing) temperature, we observe a dramatic redshift (blueshift) in the resonant frequency of the CSRR-VO_2 MM structure in a narrow temperature range in the vicinity of the transition temperature. Neither Maxwell-Garnett nor Bruggeman effective medium theory adequately describe the frequency shift and the amplitude decrease upon traversing IMT, so we employed Drude model with a significant increase of the "effective" VO_2 permittivity which provides a good match with the experimental results. Our results indicate that additional effects should be taken into account in the current effective medium theories to describe the dielectric property changes of VO_2 across the IMT. For example, additional terms need to be incorporated in the two EMTs when the particle exceeds the large size limit [46] where spatial dispersion effects should also be considered [47]. In summary, metamaterials and related metasurface constructs provide a powerful route to obtain dynamic enhancement and dielectric sensitivity that not only facilitates the development of tunable devices, but also provides a simple and effective means to interrogate the local electrodynamic properties of the materials with which they are integrated.

ACKNOWLEDGMENTS

The work at Boston university is supported by National Science Foundation under Grant No. ECCS-1810252. The work at UCSD is supported by ARO MURI Grant No. W911NF-16-1-0361. Film growth (HTZ and REH) was supported by National Science Foundation under Grant No. DMR-1352502 and the Penn State MRSEC program DMR-1420620.

Appendix A: VO_2 film growth

The VO_2 film was deposited on a sapphire substrate by hybrid molecular beam epitaxy using a combinatorial growth approach. Control over the vanadium valence state was achieved by co-supplying elemental vanadium (valence state 0) and the vanadium containing alkoxide precursor vanadium-oxo-triisopropoxide (VTIP), in which vanadium assumes the valence state 5+. Optimal flux ratios were determined using a flux gradient method to establish a valence state library across the wafer during a calibration run. Relative tuning of the two fluxes allowed straight-forward balancing of the vanadium valence state to stabilize the vanadium 4+ state. Achieving an epitaxial VO_2 film with excellent uniformity and record-high resistance change across the metal-to-insulator transition exceeding four orders of magnitude [31].

Growth was carried out in DCA M600 MBE growth chamber and VO_2 thin films were grown on a 3-inch r-cut sapphire wafer co-supply of VTIP (vacuum distilled, trace metal impurity 4N, MULTIVALENT Laboratory) using a heated gas inlet system retrofitted to an effusion cell port of the MBE growth chamber and vanadium metal (4N, Ames Laboratory) evaporated from a high temperature Knudsen cell. The respective fluxes were adjusted and maintained via a proportional-integral-derivative (PID)-controlled adjustable leak valve and capacitance manometer on the VTIP gas inlet system and PID controlled Knudsen cell temperature. The sapphire wafer was cleaned in an ultrasonic bath of acetone and then isopropanol prior to loading them into the MBE system and baked at 423 K for 2 h in the load lock chamber, subsequently transferred into the MBE growth chamber and heated to the film growth temperature of 623 K. Before deposition substrates were exposed for 20 min to an oxygen plasma (power 250 W, 910^{-7} torr oxygen background pressure). The VO_2 film were grown at a rate of about 5 min-1 in the presence of an oxygen plasma by co-supplying a vanadium atom flux of 410^{12} $cm^{-2}s^{-1}$, calibrated by a quartz crystal monitor prior to growth, and matching the required VTIP flux determined from the experimental valence state library obtained from the valence state library. After growth the VO_2 films were cooled in the presence of oxygen plasma.

Appendix B: SRR & CSRR structure

The LC resonance in a SRR structure manifests as a dip in transmission at 0.47 THz, decreasing the transmission to $\sim$0.17 when VO_2 is in insulating state, as shown in Fig. 9(a). In the metallic state, the significant increase in conductivity of the VO_2 film screens the LC resonance in the SRR structure (the metallic VO_2 shunts the capacitor of the SRR), resulting in a featureless transmission spectrum with an amplitude of $\sim$0.2. Hence, the modulation amplitude across the IMT in VO_2 is small when using a SRR structure. However, based on Babinets principle, it is possible to achieve a transmission peak with amplitude of $\sim$0.83 at almost the same frequency using the CSRR structure, as shown in Fig. 9(b). In the insulating state for the CSRR, the transmission is $\sim$0.83 decreasing to $\sim$0.14 in the metallic state. Therefore, the modulation amplitude is higher using the CSRR structure in comparison to the SRR structure.

Appendix C: Simulations based on Maxwell-Garnett and Bruggeman EMT models

We investigated effective medium dielectric functions under specific filling factors which provided the best match to the experimental terahertz transmission spectra between 335 K and 338 K. Specifically, we considered the Maxwell-Garnett and Bruggeman models. The best

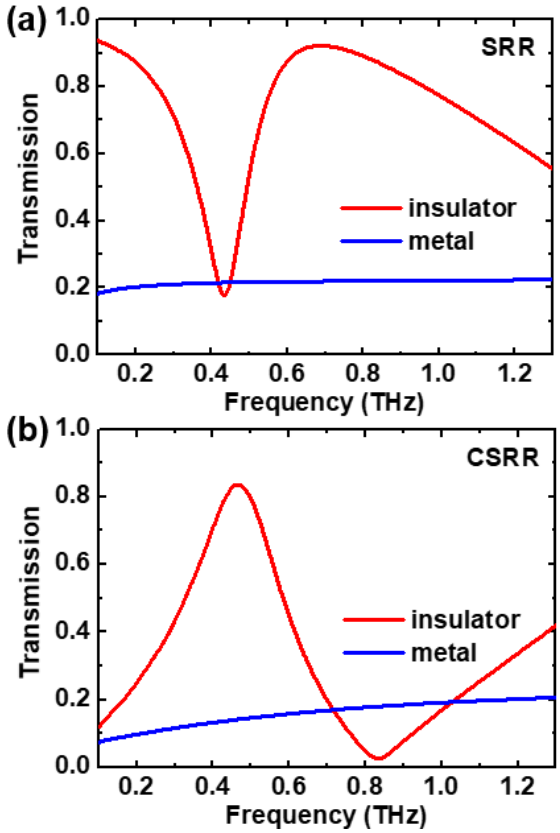


FIG. 9. Simulations of transmission spectra of (a) SRR structure and (b) CSRR structure on VO_2 film in the insulating (315 K) and metallic states (360 K).

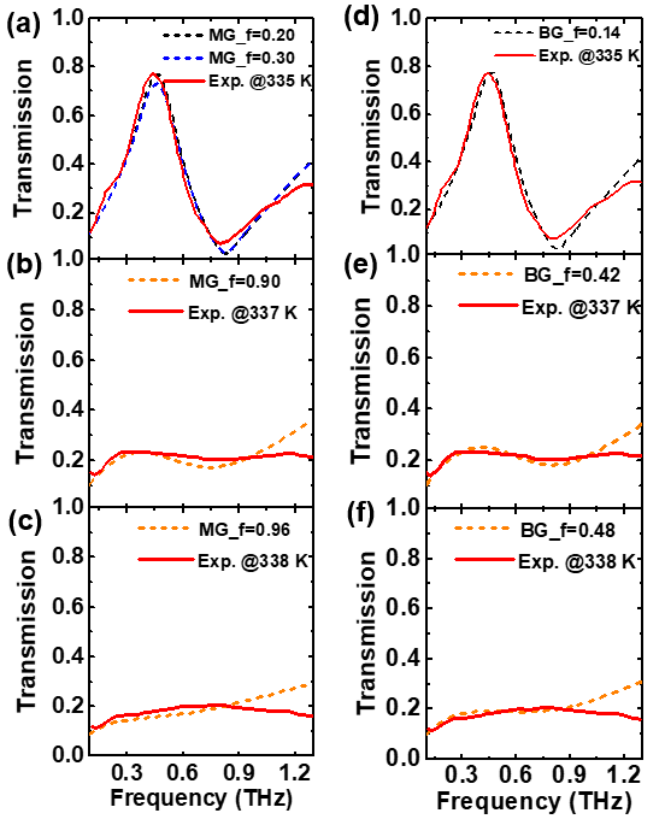


FIG. 10. Comparison between simulated (dashed lines) and experimental spectra (red lines) based on (a-c) Maxwell-Garnett EMT model and (d-f) Bruggeman EMT model. (a) and (d) are for 335 K, (b) and (d) are for 337 K and (c) and (f) are for 338 K. The corresponding filling factors are included in the insets.

simulation results at 335 K, 337 K and 338 K for the two EMT models are shown in Fig. 10 with the corresponding filling factors shown in the insets. Both EMT models manifest a the frequency shift and the amplitude change for the transmission peak at these three temperatures, with the Maxwell-Garnett model giving a much higher filling factor than the Bruggeman model. We also fitted the metallic filling factors in both EMT models with the Boltzmann relationship [28]:

$$f = f_{max}(1 - \frac{1}{1 + exp[(T - T_0)/\Delta T]}) \qquad \text{(C1)}$$

where T_0 is the transition temperature and ΔT is the transition width. The fitting curves are shown in Fig. 11, revealing that the Maxwell-Garnett model yields a higher transition temperature T_0 and a lower ΔT in comparison to the Bruggeman model. Both curves are comparable with published work [9, 48].

Appendix D: Dependence of the resonant frequency on effective mass (m^*), mobility (μ) and carrier density (n_d)

Based on the Drude model, the dielectric response of VO_2 is determined from the plasma frequency (ω_p) and scattering frequency (γ), which depend on the effective mass (m^*), mobility (μ) and carrier density (n) as described in the manuscript. During the IMT transition, m^* decreases from 7 m_0 to m_0, μ increases from 1 to 10 while n_d increases from $\sim 10^{20}$ to $\sim 10^{21}$ cm^{-3}. In Fig. 12, we show simulations of the the transmission assuming a constant ε_∞=10. Fig. 12 shows the dependence of the resonant frequency on m^* (Fig. 12(a)), μ (Fig. 11(b)), and n_d (Fig. 12(c)) while holding the other values constant. All three figures show that the resonant frequency exhibits a weak dependence on the three variables, in contrast to the experimental results. Thus, as described in the text and Figs. 4 and 8, an increase in ε_∞^{eff} during the IMT determines the redshift of the resonant frequency.

Appendix E: Conductivity calculated from the imaginary part of permittivity in simulation

Based on the parameters in Table 1, we extract the imaginary part of the permittivity at 0.5 THz from the simulation and calculated the optical conductivity [24]:

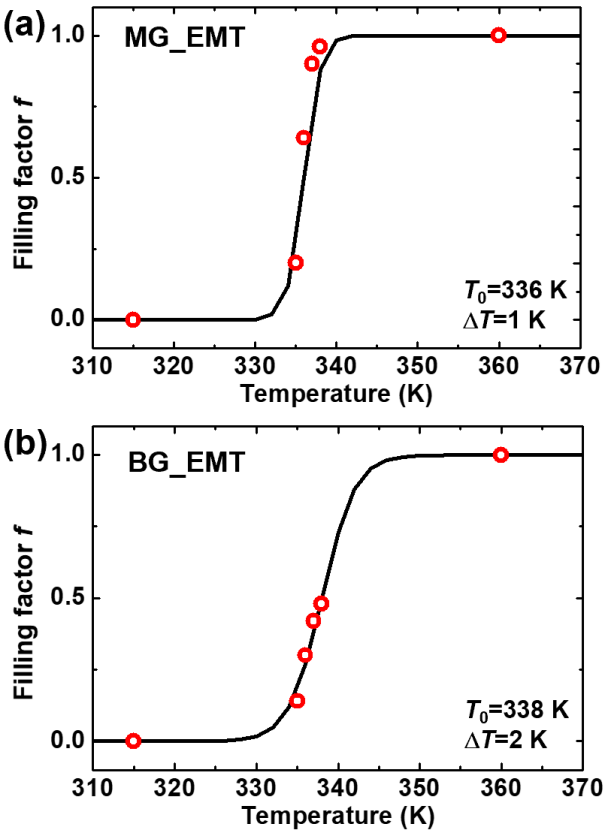


FIG. 11. The fitting curves of the filling factor dependence on temperature based on Boltzmann relation for (a) Maxwell-Garnett EMT and (b) Bruggeman EMT models.

$$\sigma_1(\omega) = \omega\varepsilon_0(\varepsilon_2 - 1) \tag{E1}$$

The results are shown in Fig. 13. The optical conductivity for VO_2 in the metallic state is $\sim$2000 Ω^{-1}cm^{-1}, which is similar to the conductivity in the published work [24].

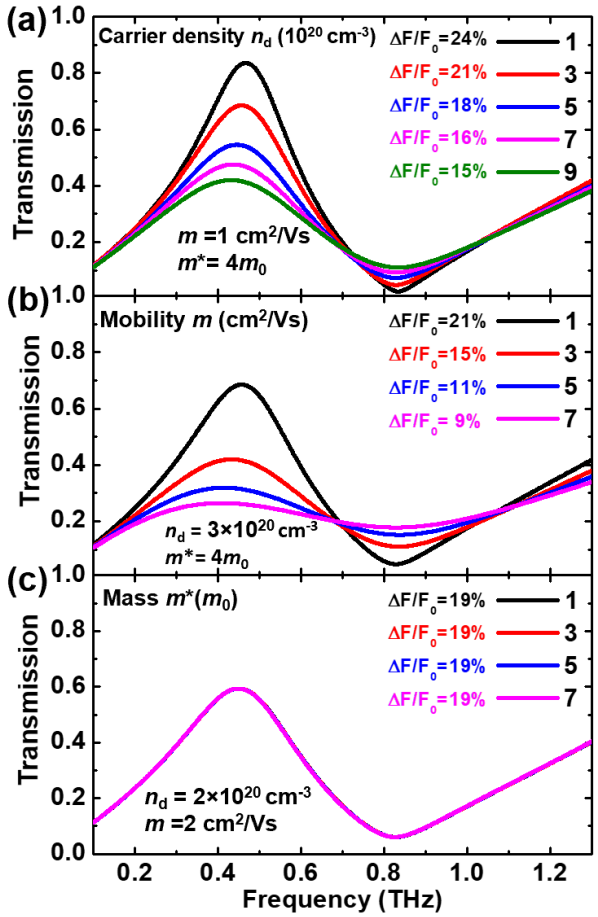


FIG. 12. Dependence of transmission of CSRR-VO_2 MM on (a) effective mass (m^*), (b) mobility (μ) and (c) carrier density (n_d). The deviations of peak frequencies between simulations and experimental results at 336 K are also included in the insets.

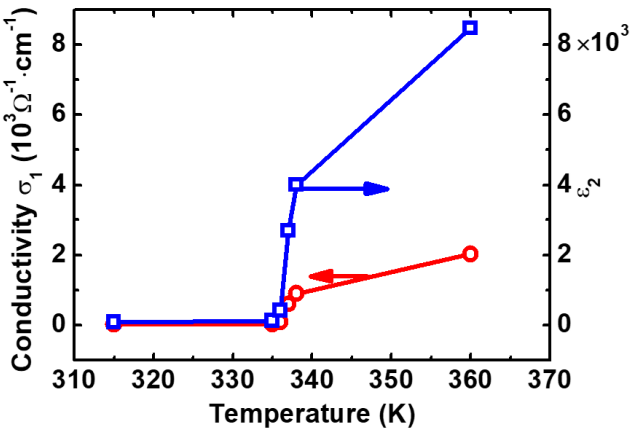


FIG. 13. Imaginary part of permittivity (ε_2) extracted from simulations and corresponding real part of conductivity (σ_1) at 0.5 THz.

[1] C. M. Watts, D. Shrekenhamer, J. Montoya, G. Lipworth, J. Hunt, T. Sleasman, S. Krishna, D. R. Smith, and W. J. Padilla, Terahertz compressive imaging with metamaterial spatial light modulators, Nat. Photonics **8**, 605 (2014).

[2] D. R. Smith, J. B. Pendry, and M. C. Wiltshire, Metamaterials and negative refractive index, Science **305**, 788 (2004).

[3] R. Maas, J. Parsons, N. Engheta, and A. Polman, Experimental realization of an epsilon-near-zero metamaterial at visible wavelengths, Nat. Photonics **7**, 907 (2013).

[4] X. Ni, Z. J. Wong, M. Mrejen, Y. Wang, and X. Zhang, An ultrathin invisibility skin cloak for visible light, Science **349**, 1310 (2015).

[5] M. Khorasaninejad and F. Capasso, Metalenses: Versatile multifunctional photonic components, Science **358** (2017).

[6] H.-T. Chen, W. J. Padilla, J. M. Zide, A. C. Gossard, A. J. Taylor, and R. D. Averitt, Active terahertz metamaterial devices, Nature **444**, 597 (2006).

[7] X. Zhao, J. Schalch, J. Zhang, H. R. Seren, G. Duan, R. D. Averitt, and X. Zhang, Electromechanically tunable metasurface transmission waveplate at terahertz frequencies, Optica **5**, 303 (2018).

[8] M. Liu, H. Y. Hwang, H. Tao, A. C. Strikwerda, K. Fan, G. R. Keiser, A. J. Sternbach, K. G. West, S. Kittiwatanakul, J. Lu, *et al.*, Terahertz-field-induced insulator-to-metal transition in vanadium dioxide metamaterial, Nature **487**, 345 (2012).

[9] K. Fan, H. Y. Hwang, M. Liu, A. C. Strikwerda, A. Sternbach, J. Zhang, X. Zhao, X. Zhang, K. A. Nelson, and R. D. Averitt, Nonlinear terahertz metamaterials via field-enhanced carrier dynamics in gaas, Phys. Rev. Lett. **110**, 217404 (2013).

[10] Y. Huang, K. Kaj, C. Chen, Z. Yang, S. R. Ul Haque, Y. Zhang, X. Zhao, R. D. Averitt, and X. Zhang, Broadband terahertz silicon membrane metasurface absorber, ACS Photonics **9**, 1150 (2022).

[11] F. Morin, Oxides which show a metal-to-insulator transition at the neel temperature, Phys. Rev. Lett. **3**, 34 (1959).

[12] J. Cao, E. Ertekin, V. Srinivasan, W. Fan, S. Huang, H. Zheng, J. Yim, D. Khanal, D. Ogletree, J. Grossman, *et al.*, Strain engineering and one-dimensional organization of metal–insulator domains in single-crystal vanadium dioxide beams, Nat. Nanotechnol. **4**, 732 (2009).

[13] B. T. Ocallahan, A. C. Jones, J. H. Park, D. H. Cobden, J. M. Atkin, and M. B. Raschke, Inhomogeneity of the ultrafast insulator-to-metal transition dynamics of vo2, Nat. Commun. **6**, 1 (2015).

[14] J. Jeong, N. Aetukuri, T. Graf, T. D. Schladt, M. G. Samant, and S. S. Parkin, Suppression of metal-insulator transition in vo2 by electric field–induced oxygen vacancy formation, Science **339**, 1402 (2013).

[15] Z. Tao, T.-R. T. Han, S. D. Mahanti, P. M. Duxbury, F. Yuan, C.-Y. Ruan, K. Wang, and J. Wu, Decoupling of structural and electronic phase transitions in vo2, Phys. Rev. Lett. **109**, 166406 (2012).

[16] H. Zhu, J. Li, L. Du, L. Shan, P. Li, X. Lu, T. Feng, S. Das, W. Huang, Q. Shi, *et al.*, Vo2-metallic hybrid metasurfaces for agile terahertz wave modulation by phase transition, APL Materials **10**, 031112 (2022).

[17] L. Liu, L. Kang, T. S. Mayer, and D. H. Werner, Hybrid metamaterials for electrically triggered multifunctional control, Nat. Commun. **7**, 1 (2016).

[18] S. Cueff, D. Li, Y. Zhou, F. J. Wong, J. A. Kurvits, S. Ramanathan, and R. Zia, Dynamic control of light emission faster than the lifetime limit using vo2 phase-change, Nat. Commun. **6**, 1 (2015).

[19] J. Li, Y. Zhang, J. Li, J. Li, Y. Yang, J. Huang, C. Ma, Z. Ma, Z. Zhang, L. Liang, *et al.*, Frequency-switchable vo2-based coding metasurfaces at the terahertz band, Optics Commun. **458**, 124744 (2020).

[20] J.-S. Li and X.-J. Li, One-dimensional terahertz dielectric gradient metasurface for broadband spoof surface plasmon polaritons couplers, Opt. Express **30**, 12823 (2022).

[21] J. Shabanpour, S. Beyraghi, and A. Cheldavi, Ultrafast reprogrammable multifunctional vanadium-dioxide-assisted metasurface for dynamic thz wavefront engineering, Sci. Rep. **10**, 1 (2020).

[22] F. Ding, S. Zhong, and S. I. Bozhevolnyi, Vanadium dioxide integrated metasurfaces with switchable functionalities at terahertz frequencies, Adv. Opt. Mater. **6**, 1701204 (2018).

[23] M. Seo, J. Kyoung, H. Park, S. Koo, H.-s. Kim, H. Bernien, B. J. Kim, J. H. Choe, Y. H. Ahn, H.-T. Kim, *et al.*, Active terahertz nanoantennas based on vo2 phase transition, Nano Lett. **10**, 2064 (2010).

[24] M. M. Qazilbash, M. Brehm, B.-G. Chae, P.-C. Ho, G. O. Andreev, B.-J. Kim, S. J. Yun, A. Balatsky, M. Maple, F. Keilmann, *et al.*, Mott transition in vo2 revealed by infrared spectroscopy and nano-imaging, Science **318**, 1750 (2007).

[25] M. M. Qazilbash, M. Brehm, G. O. Andreev, A. Frenzel, P.-C. Ho, B.-G. Chae, B.-J. Kim, S. J. Yun, H.-T. Kim, A. V. Balatsky, O. G. Shpyrko, M. B. Maple, F. Keilmann, and D. N. Basov, Infrared spectroscopy and nano-imaging of the insulator-to-metal transition in vanadium dioxide, Phys. Rev. B **79**, 075107 (2009).

[26] F. He, S. Lau, H. L. Chan, and J. Fan, High dielectric permittivity and low percolation threshold in nanocomposites based on poly (vinylidene fluoride) and exfoliated graphite nanoplates, Adv. Mater. **21**, 710 (2009).

[27] J. M. Garnett, Vii. colours in metal glasses, in metallic films, and in metallic solutions.ii, Philosophical Transactions of the Royal Society of London. Series A, Containing Papers of a Mathematical or Physical Character **205**, 237 (1906).

[28] H. Liu, Z.-H. Wang, L. Li, Y.-X. Fan, and Z.-Y. Tao, Vanadium dioxide-assisted broadband tunable terahertz metamaterial absorber, Sci. Rep. **9**, 1 (2019).

[29] P. U. Jepsen, B. M. Fischer, A. Thoman, H. Helm, J. Y. Suh, R. Lopez, and R. F. Haglund Jr, Metal-insulator phase transition in a v o 2 thin film observed with terahertz spectroscopy, Phys. Rev. B **74**, 205103 (2006).

[30] M. Brahlek, A. S. Gupta, J. Lapano, J. Roth, H.-T. Zhang, L. Zhang, R. Haislmaier, and R. Engel-Herbert, Frontiers in the growth of complex oxide thin films: past, present, and future of hybrid mbe, Adv. Funct. Mater. **28**, 1702772 (2018).

[31] H.-T. Zhang, L. Zhang, D. Mukherjee, Y.-X. Zheng, R. C. Haislmaier, N. Alem, and R. Engel-Herbert, Wafer-scale

growth of vo2 thin films using a combinatorial approach, Nat. Commun. **6**, 1 (2015).
[32] X. Zhao, J. Schalch, J. Zhang, H. R. Seren, G. Duan, R. D. Averitt, and X. Zhang, Electromechanically tunable metasurface transmission waveplate at terahertz frequencies, Optica **5**, 303 (2018).
[33] Y. Huang, Q. He, D. Zhang, and Y. Kanamori, Switchable band-pass filter for terahertz waves using vo2-based metamaterial integrated with silicon substrate, Opt. Rev. **28**, 92 (2021).
[34] T. Li, X. Luo, F. Hu, G. Li, W. Xu, Y. Zhou, Z. Wang, X. Zhang, L. Zhang, and Y. Wang, Terahertz bandstop-to-bandpass converter based on vo2 hybrid metasurface, J. Phys. D: Appl. Phys. **54**, 435105 (2021).
[35] T. Zentgraf, T. P. Meyrath, A. Seidel, S. Kaiser, H. Giessen, C. Rockstuhl, and F. Lederer, Babinets principle for optical frequency metamaterials and nanoantennas, Phys. Rev. B **76**, 033407 (2007).
[36] X. Zhao, C. Chen, K. Kaj, I. Hammock, Y. Huang, R. D. Averitt, and X. Zhang, Terahertz investigation of bound states in the continuum of metallic metasurfaces, Optica **7**, 1548 (2020).
[37] T. Cocker, L. Titova, S. Fourmaux, H.-C. Bandulet, D. Brassard, J.-C. Kieffer, M. El Khakani, and F. Hegmann, Phase diagram of the ultrafast photoinduced insulator-metal transition in vanadium dioxide, Appl. Phys. Lett. **97**, 221905 (2010).
[38] C. Berglund and H. Guggenheim, Electronic properties of vo2 near the semiconductor-metal transition, Phys. Rev. **185**, 1022 (1969).
[39] T. C. Choy, *Effective medium theory: principles and applications*, Vol. 165 (Oxford University Press, 2015).
[40] N. Émond, B. Torriss, D. Morris, and M. Chaker, Natural metamaterial behavior across the phase transition for wxv1- xo2 films revealed by terahertz spectroscopy, Acta Mater. **140**, 20 (2017).
[41] J. H. Park, J. M. Coy, T. S. Kasirga, C. Huang, Z. Fei, S. Hunter, and D. H. Cobden, Measurement of a solid-state triple point at the metal–insulator transition in vo2, Nature **500**, 431 (2013).
[42] A. Litvinchuk, C. Chen, N. Kolev, V. Popov, V. Hadjiev, M. Iliev, R. Bontchev, and A. Jacobson, Optical properties of high-dielectric-constant cacu3ti4o12 films, Phys. Status Solidi A **195**, 453 (2003).
[43] Z.-M. Dang, J.-K. Yuan, S.-H. Yao, and R.-J. Liao, Flexible nanodielectric materials with high permittivity for power energy storage, Adv. Mater. **25**, 6334 (2013).
[44] P. Lunkenheimer, V. Bobnar, A. V. Pronin, A. I. Ritus, A. A. Volkov, and A. Loidl, Origin of apparent colossal dielectric constants, Phys. Rev. B **66**, 052105 (2002).
[45] J. Liu, C.-G. Duan, W.-G. Yin, W.-N. Mei, R. W. Smith, and J. R. Hardy, Large dielectric constant and maxwell-wagner relaxation in bi 2/ 3 cu 3 ti 4 o 12, Physical review B **70**, 144106 (2004).
[46] G. A. Niklasson, C. Granqvist, and O. Hunderi, Effective medium models for the optical properties of inhomogeneous materials, Appl. Opt. **20**, 26 (1981).
[47] A. Moradi, Maxwell-garnett effective medium theory: Quantum nonlocal effects, Phys. Plasmas **22**, 042105 (2015).
[48] A. R. Gentle, G. B. Smith, and A. I. Maaroof, Frequency and percolation dependence of the observed phase transition in nanostructured and doped vo2 thin films, J. Nanophotonics **3**, 031505 (2009).
[49] C.-W. Nan, Y. Shen, and J. Ma, Physical properties of composites near percolation, Annu. Rev. Mater. Sci. **40**, 131 (2010).
[50] M. K. Liu, M. Wagner, E. Abreu, S. Kittiwatanakul, A. McLeod, Z. Fei, M. Goldflam, S. Dai, M. M. Fogler, J. Lu, S. A. Wolf, R. D. Averitt, and D. N. Basov, Symmetry breaking and geometric confinement in vo2: Results from a three-dimensional infrared nano-imaging, Phys. Rev. Lett. **111**, 096602 (2013).
[51] D. J. Hilton, R. P. Prasankumar, S. Fourmaux, A. Cavalleri, D. Brassard, M. A. El Khakani, J. C. Kieffer, A. J. Taylor, and R. D. Averitt, Enhanced photosusceptibility near t c for the light-induced insulator-to-metal phase transition in vanadium dioxide, Phys. Rev. Lett. **99**, 226401 (2007).